



Dynamic modeling and simulation of hydrotreating of gas oil obtained from heavy crude oil

Fabián S. Mederos^{a,1}, Jorge Ancheyta^{a,b,*,1,2}, Ignacio Elizalde^{a,b,1,2}

^a Instituto Mexicano del Petróleo (IMP), Eje Central Lázaro Cárdenas Norte 152, Col. San Bartolo Atepehuacan, México, DF 07730, Mexico

^b Escuela Superior de Ingeniería Química e Industrias Extractivas (ESIQIE-IPN), UPALM, Zacatenco, México, DF 07738, Mexico

ARTICLE INFO

Article history:

Received 24 August 2011

Received in revised form 3 February 2012

Accepted 10 February 2012

Available online 10 March 2012

Keywords:

Dynamic modeling
Catalytic hydrotreating
Trickle-bed reactor

ABSTRACT

This paper describes a dynamic heterogeneous one-dimensional model of trickle-bed reactor used for catalytic hydrotreating of oil fractions. The model takes into consideration the main reactions occurring in the hydrotreating process: hydrosulfurization, hydrodenitrogenation, hydrodearomatization (mono-, di-, and polyaromatics), olefins hydrogenation, and mild hydrocracking (gas oil, naphtha, and gases). Kinetic parameters were determined from experimental data obtained in an isothermal bench-scale reactor during hydrotreating of atmospheric gas oil coming from a heavy crude oil over a commercial CoMo catalyst. The developed model was used to predict the dynamic behavior of an industrial hydrotreating reactor within a wide range of reaction conditions. Changes in concentration, partial pressure, and temperature profiles are simulated and discussed as a function of reactor axial position and time. The simulation results obtained with the proposed dynamic model showed good agreement with experimental data.

© 2012 Elsevier B.V. All rights reserved.

1. Introduction

Catalytic hydrotreating (HDT) has become one of the fundamental processes in the petroleum-refining industry from technical, economic, and environmental points of view. The HDT process has been used for over 60 years to obtain fuels with improved quality and low polluting compounds content (sulfur, nitrogen, aromatics, etc.) and to fulfill the applicable legal norms of gas emissions. Nevertheless, since 2009 in the European Union automotive fuels have to meet the so-called ultra-low sulfur specifications (10 ppmw total sulfur in gasoline and diesel), which are probably to be applied worldwide [1]. Among other changes (i.e., new reactor design, use of new generation catalysts, etc.), these environmental restrictions will force the refineries to increase the severity in the operating conditions of the HDT reactor in order to match these more stringent specifications [2–4]. To reach this low sulfur content value is even more complicated when refinery feed is composed by high amount of heavy crude oil. Distillates, such as gas oil, coming from heavy petroleum are characterized by high content of impurities

(sulfur, nitrogen, aromatics, etc.) exhibiting complex structure and refractory in nature. These new conditions will alter the performance of HDT commercial units; for instance, light hydrocarbons production, H₂ consumption, yield of liquid, temperature gradient in the reactor will be altered, among other consequences. One way to deal with this situation is either by detailed and extensive experimental program or by reactor modeling and simulation, which allows for having a deep understanding on the phenomena occurring in the HDT reactor with the main purpose of establishing the optimal operating conditions, catalyst formulation, process configuration, reactor design, feed selection, reactor internals design, effect of operating variables, combination with other emerging technologies, etc.

Among the different approaches for modeling chemical reactors sustaining HDT reactions, the most common are those that perform the analysis based on local average behavior of molecules (lump models), which generally were developed as pseudohomogeneous and heterogeneous reactor models on steady state [5–21], while studies on dynamic modeling and simulation with either pseudo-homogeneous or heterogeneous reactor models are scarce [22–29], and nothing has been reported for modeling the hydrotreating of gas oil distilled from heavy petroleum.

The objective of the present contribution is to illustrate the application of a dynamic plug-flow heterogeneous one-dimensional trickle-bed reactor (TBR) model to obtain kinetic data from bench-scale experiments and their subsequent use to predict the unsteady state behavior of an industrial HDT reactor.

* Corresponding author at: Instituto Mexicano del Petróleo, Eje Central Lázaro Cárdenas 152, Col. San Bartolo Atepehuacan, Mexico City 07730, Mexico. Tel.: +52 55 9175 8443; fax: +52 55 9175 8429.

E-mail address: jancheyt@imp.mx (J. Ancheyta).

¹ IMP.

² ESIQIE-IPN.

Nomenclature

a_L	gas–liquid interfacial area per unit reactor volume, $\text{cm}_f^2/\text{cm}_r^3$
a_S	liquid–solid interfacial area per unit reactor volume, $\text{cm}_S^2/\text{cm}_r^3$
A', b'	empirical constants for Bondi's correlation, dimensionless
C_{pf}	specific heat capacity of f phase, $\text{J}/(\text{g}_f \text{K})$
C_i^L	molar concentration of component i in the bulk liquid phase, $\text{mol}_i/\text{cm}_L^3$
C_{SLi}^S	molar concentration of compound i at surface of solid covered by liquid phase, $\text{mol}_i/\text{cm}_L^3$
d_{pe}	equivalent particle diameter, cm_S
D_{ei}^L	effective fickian diffusivity in liquid phase of compound i inside porous solid, $\text{cm}_L^3/(\text{cm}_S \text{ s})$
D_{Mi}^L	molecular diffusion coefficient of compound i in the liquid phase, $\text{cm}_L^3/(\text{cm}_S \text{ s})$
E_{aj}	activation energy for j reaction, J/mol_i
f_w	catalyst wetting efficiency, $\text{cm}_{S, \text{wet}}^2/\text{cm}_S^2$
F	objective function to be optimized, $\text{mol}_i/\text{cm}_L^3$ or $\text{g}_i/\text{g}_{\text{Total}}$
G_{mL}	superficial mass flow velocity of liquid phase, $\text{g}_L/(\text{cm}_f^2 \text{ s})$
h_{LS}	heat transfer coefficient for liquid film surrounding the catalyst particle, $\text{J}/(\text{s cm}_S^2 \text{ K})$
H_i	Henry's law coefficient of component i , $\text{MPa cm}_L^3/\text{mol}_i$
$k_{1,2,3}$	intrinsic reaction rate constants for mild HCR reactions, $(\text{mol}_i/\text{cm}_L^3)^{1-n} (1/\text{s})$
$k'_{\text{app},j}$	apparent reaction rate constant for heterogeneous reaction j , $(\text{cm}_L^3)^{m+n}/[\text{mol}_i^{(m+n-1)} \text{g}_S \text{ s}]$
$k'_{\text{in},j}$	intrinsic reaction rate constant for heterogeneous reaction j , $(\text{cm}_L^3)^{m+n}/[\text{mol}_i^{(m+n-1)} \text{g}_S \text{ s}]$
$k_{0,j}$	frequency factor for reaction j , $(\text{mol}_i/\text{cm}_L^3)^{1-n} (1/\text{s})$
$k'_{0,j}$	frequency factor for heterogeneous reaction j , $(\text{cm}_L^3)^{m+n}/[\text{mol}_i^{(m+n-1)} \text{g}_S \text{ s}]$
k_i^S	liquid–solid mass transfer coefficient of compound i , $\text{cm}_L^3/(\text{cm}_S^2 \text{ s})$
K_{Li}	overall gas–liquid mass transfer coefficient of compound i in the liquid phase, $\text{cm}_L^3/(\text{cm}_f^2 \text{ s})$
K_j	equilibrium constant for j ($=\text{HDA}_{\text{Poly}}/\text{Di}/\text{Mono}$) reaction, dimensionless
$K_{\text{H}_2\text{S}}$	adsorption–equilibrium constant of H_2S on catalyst active sites, $\text{cm}_L^3/\text{mol}_{\text{H}_2\text{S}}$
$K_{0,j}$	pre-exponential factor for equilibrium constant of reaction j , dimensionless
$K_{0,\text{H}_2\text{S}}$	pre-exponential factor for adsorption–equilibrium of H_2S , $\text{cm}_L^3/\text{mol}_{\text{H}_2\text{S}}$
L_B	length of catalyst bed, cm_r
m, n	reaction order, dimensionless
MW_L	molecular weight of liquid phase, g_L/mol_L
N_{RL}	number of reactions in the liquid phase, dimensionless
p_i^G	partial pressure of component i in the bulk gas phase, MPa
r_j^L	rate of reaction j per unit of volume in the liquid phase, $\text{mol}_i/(\text{cm}_L^3 \text{ s})$
$r_j'^L$	rate of reaction j per unit of catalyst mass in the liquid phase, $\text{mol}_i/(\text{g}_S \text{ s})$
R	gas law constant, $\text{J}/(\text{mol}_i \text{ K})$

S_p	total geometric external surface area of catalyst particle, cm_S^2
t	time, s
T_f	temperature of f phase, K
u_f	superficial velocity of f phase, $\text{cm}_f^3/(\text{cm}_r^2 \text{ s})$
V_p	total geometric volume of catalyst particle, cm_S^3
w_i	weight fraction of compound i in the liquid phase, g_i/g_L
Y_i	weight fraction for mild HCR reactions, $\text{g}_i/\text{g}_{\text{Total}}$
z	axial reactor coordinate, cm_r

Greek symbols

$\Delta H_{\text{ads}, \text{H}_2\text{S}}$	adsorption enthalpy of H_2S , $\text{J}/\text{mol}_{\text{H}_2\text{S}}$
$\Delta H_{R,j}^L$	heat of reaction j in the liquid phase, J/mol_i
ϵ_B	catalyst bed void fraction, $\text{cm}_{(G+L)}^3/\text{cm}_r^3$
ϵ_S	catalyst particle porosity, $\text{cm}_{(G+L)}^3/\text{cm}_S^3$
ϵ_f	external holdup of f phase, $\text{cm}_f^3/\text{cm}_r^3$
η_j^L	catalyst effectiveness factor of reaction j in the liquid phase, dimensionless
ρ_B	catalyst bed density, $\text{g}_S/\text{cm}_{\text{cat}}^3$
ρ_f	density of f phase at process conditions, g_f/cm_f^3
ν_{ij}^L	stoichiometric coefficient of component i in reaction j in the liquid phase, dimensionless
ζ	catalyst bed dilution factor, $\text{cm}_{\text{cat}}^3/(\text{cm}_{\text{cat}}^3 + \text{cm}_{\text{inert}}^3)$
ϕ_S	shape factor ($=\text{surface area of a sphere of equal volume}/\text{solid surface area}$), dimensionless
Φ_j^L	Thiele modulus of reaction j in the liquid phase, dimensionless
τ	tortuosity factor for catalyst particle, cm_L/cm_S

Subscripts

app	apparent
calc	calculated
CH_4	methane
Di	diaromatics
exp	experimental
f	phase (gas, liquid or solid); final or outlet condition
G	gas phase
GO	gas oil
HC	hydrocarbon
HCR	hydrocracking reaction
HDA	hydrodearomatization reaction
HDN	hydrodenitrogenation reaction
HDS	hydrodesulfurization reaction
HGO	olefins hydrogenation reaction
H_2	molecular hydrogen
H_2S	hydrogen sulfide
i	component index
in	intrinsic
L	gas–liquid interface
j	reaction index
k	experiment index
L	liquid phase
Mono	monoaromatics
N	nitrogen compound
Naph	naphthenes
NH_3	ammonia
O	olefins
Poly	polyaromatics
S	sulfur compound; solid phase; condition at external surface of catalyst particle
0	initial or inlet condition; reference condition

Superscripts

G	gas phase; gas-side of the gas–liquid interface
L	liquid phase; liquid-side of the gas–liquid interface
S	solid phase; liquid–solid interface

2. Experimental**2.1. Materials and experimental setup**

The feed used for all experiments was a straight-run gas oil obtained from a heavy crude oil, whose properties are presented in Table 1. The commercial catalyst used for experiments was a pre-sulfided cobalt molybdenum supported on γ -alumina. The reactor was loaded with 99.43 g (100 ml) of powdered catalyst previously crushed and sieved, which properties are given in Table 1.

The bench-scale reactor is operated in downflow and isothermal mode provided with independent temperature control of a three-zone electric furnace. The internal diameter of the reactor is 2.54 cm and at the center a thermowell of external diameter of 0.635 cm was placed. Catalytic length was of 25.2 cm.

2.2. Experimental tests

Prior to experimental runs, the catalyst was activated by the procedure reported elsewhere [30]. After catalyst sulfiding, the experiments were carried out at constant pressure of 5.3 MPa and H_2 /oil ratio of 356 std m^3/m^3 (2000 scf/bbl), varying the reactor temperature from 340 to 380 °C and liquid hourly space

velocity (LHSV) from 1 to 3 h^{-1} . Product samples were collected under steady-state operation at 6 h intervals after allowing a 4 h stabilization period between experimental runs.

2.3. Analytical methods

The atmospheric gas oil feed and liquid product samples were characterized using the following techniques.

The sulfur content was measured by an X-ray fluorescence spectrometer following the ASTM D-4294 method. Before sulfur analyzes the hydrotreated samples were treated (purged) with nitrogen gas in order to strip dissolved H_2S and NH_3 . The total nitrogen content was determined using a chemiluminescence method as per ASTM D-4629, while the basic nitrogen content was determined by the color indicator titration method (UOP-313).

The FIA (ASTM D-1319) method was used to separate feed and liquid product samples into saturate and aromatic fractions. The aromatic part in liquid samples was analyzed by supercritical fluid chromatography according to ASTM D-5186 method in order to obtain the content of aromatic structures (poly-, di-, and monoaromatics). The saturate fraction of the feed was used to measure the initial naphthenes content by field-desorption mass spectrometry according to ASTM D-2425 method.

The extent of hydrocracking (HCR) of gas oil to lighter products was determined through material balance and gas chromatographic analysis of gas and liquid product samples. The bromine number was determined by ASTM D-1159 and the olefin content was estimated from the bromine number.

Other physical properties of the feed and products were determined by standard methods: liquid density by U-tube density cell according to ASTM D-4052 method, viscosity by a Stabinger viscosity cell based on ASTM D-7042 method, and boiling point distribution by ASTM D-86 method. The gas product was analyzed by on-line gas chromatograph. Physical properties of the catalyst such as bulk density of aggregates and total pore volume using the Brunauer–Emmett–Teller (BET) technique were determined by ASTM C-29 and ASTM-4222 methods, respectively.

3. Formulation of the reactor model

The model developed to simulate a TBR for HDT of oil fractions at bench and commercial scales is dynamic one-dimensional heterogeneous, which is based on the three-phase steady-state reactor model reported in the literature [11,18].

3.1. Assumptions

In the present work the following assumptions were made:

1. The reactors (bench and commercial) operate in dynamic regime.
2. Both gas and liquid phases behave as plug flow.
3. The bench-scale reactor is isothermally and isobarically operated.
4. The commercial adiabatic reactor is isothermal only in the radial direction.
5. No liquid evaporation or vapor condensation along the catalytic bed.
6. In the bench-scale reactor the gas-side of the gas–liquid mass transfer resistance is assumed to be negligible.
7. Liquid–solid film mass transfer is the rate limiting resistance in bench-scale reactor, while intraparticle mass transfer is the rate limiting resistance in commercial reactor.
8. Effectiveness factors are used to estimate the intraparticle mass transfer resistances in commercial reactor.

Table 1
Properties of the gas oil feedstock and catalyst.

Gas Oil	Value	
Density		
at 15.6 °C and 586 mmHg (g/cm ³)		0.873
at 20 °C and 586 mmHg (g/cm ³)		0.869
Viscosity		
at 20 °C and 586 mmHg (cP)		7.2554
at 40 °C and 586 mmHg (cP)		4.0161
at 60 °C and 586 mmHg (cP)		2.5455
Total sulfur (wt%)		2.19
Total nitrogen (wppm)	330	
Basic nitrogen (wppm)	136	
Nonbasic nitrogen (wppm)	194	
Olefins (wt%)	4.83	
Total aromatics (wt%)	34.9	
Polyaromatics (wt%)	6.6	
Diaromatics (wt%)	7.8	
Monoaromatics (wt%)	20.5	
Total saturates (wt%)	65.1	
Naphthenes (wt%)	46.17	
Paraffins (wt%)	18.93	
Atmospheric distillation (°C)		
IBP	284.8	
5 vol%	291.4	
10 vol%	292.8	
90 vol%	318.8	
95 vol%	323.7	
FBP	328.7	
Catalyst ^a		
Co (wt%)	3.47	
Mo (wt%)	14.70	
γ -Al ₂ O ₃ (wt%)	81.83	
Particle shape	Crushed	Trilobe extrudate
Equivalent particle diameter (cm)	0.0230	0.2540
Bulk density (g/cm ³)	0.9943	0.9200

^a Sulfided catalyst; crushed particles sieved with 60/70 mesh size.

9. Chemical reactions occur only in the liquid phase when contacting with the solid phase surface.
10. The liquid volume (or liquid holdup) in the bench-scale and commercial reactors remains constant.
11. The catalyst particles are completely wetted in the commercial reactor.
12. Catalyst activity does not change with time because of the use of fresh catalyst and the relatively short time required during experiments.
13. There are not intraparticle temperature differences (isothermal solid phase).
14. The energy balance for gas phase is not taken into consideration because the heat capacity of the gas phase is much lower compared with that of the liquid phase.

Regarding assumption 5, it should be mentioned that modeling the feed vaporization in TBRs is in fact a difficult task. Up until now, only one paper dealing with this issue has used this concept in simulations of hydrotreating reactor [31]. In that study the authors have concluded that only slight differences are found in temperature and hydrodearomatization profiles by considering the vaporization of hydrocarbon (vapor liquid equilibrium, VLE). Also although they have found that hydrodesulfurization within the reactor can be significant, the effect of vaporization becomes smaller for high levels of conversion. Higher HDS is predicted by using VLE calculations, which provokes an increase in temperature with the consequent enhanced vaporization. Hence these phenomena are strongly linked, and ignoring them may cancel its effect. This is in agreement with theoretical calculations of Akgerman et al. [32] who pointed out that at high conversions, the difference between the model that takes into account the volatiles and that that does not diminishes due to depletion of the limiting reactant. In our study the level of HDS was greater than 95%, thus according to these previous reports, the effect of vaporization is expected to be minimal. In addition, the feed used in our experiments is heavy oil-derived gas oil, which apart from exhibiting high contents of sulfur and aromatics, such compounds are of high-molecular weight as compared with those present in typical gas oil. This heaviness and complexity of these impurities make our feedstock of less volatility. In summary, although VLE calculations are welcomed the assumption that liquid and gas phase are in equilibrium is not well established [7].

3.2. Unsteady state mass balances

The mass transfer of the compounds in the TBR is described with the following set of partial differential equations (PDEs), taking into account the previous assumptions.

3.2.1. Gas phase

The unsteady state mass-balance equation in the catalyst bed for the compounds present in the gas phase is the following:

$$\frac{\varepsilon_G}{RT_L} \frac{\partial p_i^G}{\partial t} = \pm \frac{u_G}{RT_L} \frac{\partial p_i^G}{\partial z} - K_{Li} a_L \left(\frac{p_i^G}{H_i} - C_i^L \right) \quad (1)$$

where $i = H_2, H_2S, NH_3$, and CH_4 . “–” sign is for cocurrent operation and the “+” sign is for countercurrent operation.

3.2.2. Liquid phase

The unsteady state mass-balance equation in the catalyst bed for the gaseous compounds in the liquid phase is

$$\varepsilon_L \frac{\partial C_i^L}{\partial t} = -u_L \frac{\partial C_i^L}{\partial z} + K_{Li} a_L \left(\frac{p_i^G}{H_i} - C_i^L \right) - k_i^S a_S (C_i^L - C_{SLi}^S) \quad (2)$$

where $i = H_2, H_2S, NH_3$, and CH_4 .

The model assumes that the organosulfur, organonitrogen, aromatic, and olefin compounds, as well as the liquid hydrocarbons, are nonvolatile; therefore, the unsteady state mass-balance for the liquid compounds is

$$\varepsilon_L \frac{\partial C_i^L}{\partial t} = -u_L \frac{\partial C_i^L}{\partial z} - k_i^S a_S (C_i^L - C_{SLi}^S) \quad (3)$$

where $i = S, N, Poly, Di, Mono, Naph, O, GO$, and *Naphtha*.

3.2.3. Solid phase

The components transported between liquid and solid phases are consumed or produced by the chemical reaction at the wet catalyst surface, according to the following first-order ordinary differential equations (ODEs):

$$\varepsilon_S (1 - \varepsilon_B) \frac{\partial C_{SLi}^S}{\partial t} = k_i^S a_S (C_i^L - C_{SLi}^S) + f_w \rho_B \zeta \sum_{j=1}^{N_{RL}} v_{i,j}^L \eta_j^L r_j^L (C_{SLi}^S, T_S^S) \quad (4)$$

where $i = H_2, H_2S, NH_3, CH_4, S, N, Poly, Di, Mono, Naph, O, GO$, and *Naphtha*; $j = HDS, HDN, HDA_{Poly}, HDA_{Di}, HDA_{Mono}, HDA_{Naph}, HGO$, and *HCR*.

3.3. Unsteady state heat balances

Since the HDT reactions are exothermic in nature, the energy-balance equations for commercial HDT reactor modeling operating under adiabatic no isothermal conditions are given by the following terms [7]:

(i) Liquid phase

$$\varepsilon_L \rho_L C_{pL} \frac{\partial T_L}{\partial t} = -u_L \rho_L C_{pL} \frac{\partial T_L}{\partial z} - h_{LS} a_S (T_L - T_S^S) \quad (5)$$

(ii) Solid phase

$$\varepsilon_S \rho_S C_{pS} \frac{\partial T_S^S}{\partial t} = h_{LS} a_S (T_L - T_S^S) + f_w \rho_B \sum_{j=1}^{N_{RL}} \eta_j^L r_j^L (C_{SLi}^S, T_S^S) (-\Delta H_{R,j}^L) \quad (6)$$

3.4. Boundary conditions

Since the mathematical model is a system of PDEs and ODEs with time and spatial coordinate as independent variables, it is necessary to define the following initial and boundary conditions for the gas, liquid, and solid phases for cocurrent operation mode:

(i) Initial conditions:

$$\begin{aligned} \text{For } t = 0, \quad \text{at } z = 0, \quad p_i^G &= (p_i^G)_0, \quad i = H_2, H_2S, NH_3, \quad \text{and } CH_4 \\ C_i^L &= (C_i^L)_0 \quad \text{and} \\ C_{SLi}^S &= 0, \quad i = H_2, H_2S, NH_3, CH_4, S, N, Poly, Di, Mono, Naph, O, GO, \quad \text{and } Naphtha \\ T_L &= T_S^S = T_0 \end{aligned} \quad (7)$$

$$\begin{aligned} \text{at } 0 < z < L_B, \quad p_i^G = 0, \quad i = \text{H}_2, \text{H}_2\text{S}, \text{NH}_3, \quad \text{and } \text{CH}_4 \\ C_i^L = 0 \quad \text{and} \\ C_{SLi}^S = 0, \quad i = \text{H}_2, \text{H}_2\text{S}, \text{NH}_3, \text{CH}_4, \text{S}, \text{N}, \text{Poly}, \text{Di}, \text{Mono}, \text{Naph}, \text{O}, \text{GO}, \quad \text{and } \text{Naphtha} \\ T_L = T_S^S = T_0 \end{aligned} \quad (8)$$

$$\begin{aligned} \text{at } z = L_B, \quad p_i^G = 0, \quad i = \text{H}_2, \text{H}_2\text{S}, \text{NH}_3, \quad \text{and } \text{CH}_4 \\ C_i^L = 0 \quad \text{and} \\ C_{SLi}^S = 0, \quad i = \text{H}_2, \text{H}_2\text{S}, \text{NH}_3, \text{CH}_4, \text{S}, \text{N}, \text{Poly}, \text{Di}, \text{Mono}, \text{Naph}, \text{O}, \text{GO}, \quad \text{and } \text{Naphtha} \\ T_L = T_S^S = T_0 \end{aligned} \quad (9)$$

(ii) Boundary conditions:

$$\begin{aligned} \text{For } t > 0 \quad \text{at } z = 0, \quad p_i^G = (p_i^G)_0, \quad i = \text{H}_2, \text{H}_2\text{S}, \text{NH}_3, \quad \text{and } \text{CH}_4 \\ C_i^L = (C_i^L)_0 \quad \text{and } C_{SLi}^S = 0, \\ i = \text{H}_2, \text{H}_2\text{S}, \text{NH}_3, \text{CH}_4, \text{S}, \text{N}, \text{Poly}, \text{Di}, \text{Mono}, \text{Naph}, \text{O}, \text{GO}, \quad \text{and } \text{Naphtha} \\ T_L = (T_L)_0; \quad T_S^S = (T_S^S)_0 \end{aligned} \quad (10)$$

When a high-purity hydrogen stream without gas recycle is used, such as in the case of laboratory reactor, or when the recycle gas has been subject to purification process in commercial HDT units, the values of partial pressures (p_i^G) and liquid molar concentrations (C_i^L) of H_2S , NH_3 , and CH_4 at the entrance of the catalytic bed ($z=0$) are equal or very close to zero.

3.5. Integration method

The reactor model was solved numerically by applying the method of lines [33,34]. The set of PDEs describing the mass and heat transfer in the reactor were transformed into a set of first-order ODEs by discretizing the spatial partial derivatives in the axial direction using the backward finite difference expressions and leaving the independent variable time (time partial derivatives) without discretize. The final system of ODEs obtained was then solved with respect to time using the fourth-order Runge-Kutta method. The software developed in this work to calculate the chemical-physical properties, transport properties, hydrodynamic parameters and simultaneously to solve the system of ODEs was a stand-alone program coded in Visual Fortran 90 programming language that can be run on a personal computer.

3.6. Reaction kinetic models

3.6.1. Hydrodesulfurization reaction

To model hydrodesulfurization (HDS) reaction the following generalized representation was assumed:



where Ar-S is the sulfur-containing compound, H_2 is hydrogen, Ar-H is the corresponding aromatic compound free of sulfur, and H_2S is hydrogen sulfide. The kinetic model to describe the HDS reaction in this work is based on the following previously reported equation:

$$r'_{\text{HDS}} = \frac{k'_{\text{in,HDS}} (C_{\text{SLS}}^S)^{m_1} (C_{\text{SLH}_2}^S)^{m_2}}{(1 + K_{\text{H}_2\text{S}} C_{\text{SLH}_2\text{S}}^S)^2} \quad (12)$$

The exponent two in the denominator of Eq. (12) means the number of active sites participating in adsorption for hydrogen sulfide. The adsorption equilibrium constant of hydrogen sulfide ($K_{\text{H}_2\text{S}}$) is also a function of temperature and can be estimated using the van't Hoff equation:

$$K_{\text{H}_2\text{S}} = K_{0,\text{H}_2\text{S}} \exp \left(\frac{\Delta H_{\text{ads,H}_2\text{S}}}{RT_S^S} \right) \quad (13)$$

3.6.2. Hydrodenitrogenation reaction

As in the case of HDS reaction, all the organic nitrogen compounds in the feedstock are grouped in one lump. The following generalized stoichiometric equation was used to represent all hydrodenitrogenation (HDN) reactions:



where Ar-N is the nitrogen-bearing compound, Ar-H is the aromatic compound free of nitrogen, and NH_3 is ammonia. The following pseudo-first-order kinetics with respect to the concentration of total nitrogen was assumed for the HDN reaction [14]:

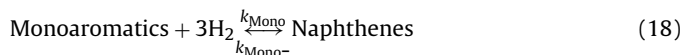
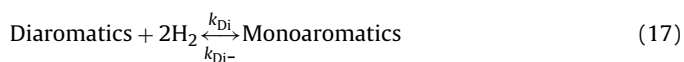
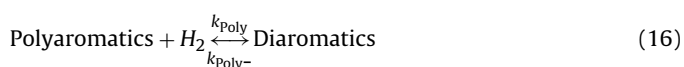
$$r_{\text{HDN}}^L = \frac{\rho_B r_{\text{HDN}}^L}{[\epsilon_S(1 - \epsilon_B)]} = k_{\text{in,HDN}} (C_{\text{SLN}}^S) \quad (15)$$

Although nitrogen compounds can influence HDS activity due to competitive adsorption, that effect was not considered in this study by the following reasons:

- The heavy oil-derived gas oil used in our experiments possesses much lower nitrogen content in comparison with sulfur and aromatics.
- The CoMo supported catalyst used for the test is more selective for sulfur removal.
- The effect of nitrogen compounds on HDS and other reactions is more notorious when dealing with studies for producing ultra-low sulfur diesel, which is not our case. Only in such cases the competitive adsorption of nitrogen on HDS is important [37].

3.6.3. Hydrodearomatization reaction

The HDA reactions network was modeled with the following stoichiometric equations as reported by Chowdhury et al. [5]:



It is reported in the literature that in multiring aromatic compounds, the ring with the lowest aromaticity is first hydrogenated. For instance the low aromaticity character of anthracene middle ring causes this compound to be hydrogenated to produce 9,10-dihydroanthracene, and phenanthrene is hydrogenated to 9,10-dihydrophenanthrene over NiMo/alumina catalyst [35,36]. Based on these experimental evidences, Chowdhury et al. [5] formulate Eq. (16), which was also used for our model.

The HDA reaction rates are expressed as [15]:

$$r_{\text{HDA}_{\text{Poly}}}^L = k_{\text{in,HDA}_{\text{Poly}}}^* (p_{\text{H}_2}^G)^{n_1} (C_{\text{SLPoly}}^S) - k'_{\text{in,HDA}_{\text{Poly}}} (C_{\text{SLDi}}^S) \quad (19a)$$

$$r_{\text{HDA}_{\text{Di}}}^L = -k_{\text{in,HDA}_{\text{Poly}}}^* (p_{\text{H}_2}^G)^{n_1} (C_{\text{SLPoly}}^S) + k'_{\text{in,HDA}_{\text{Poly}}} (C_{\text{SLDi}}^S) + k_{\text{in,HDA}_{\text{Di}}}^* (p_{\text{H}_2}^G)^{n_2} (C_{\text{SLDi}}^S) - k'_{\text{in,HDA}_{\text{Di}}} (C_{\text{SLMono}}^S) \quad (20a)$$

$$r_{\text{HDA}_{\text{Mono}}}^L = -k_{\text{in,HDA}_{\text{Di}}}^* (p_{\text{H}_2}^G)^{n_2} (C_{\text{SLDi}}^S) + k'_{\text{in,HDA}_{\text{Di}}} (C_{\text{SLMono}}^S) + k_{\text{in,HDA}_{\text{Mono}}}^* (p_{\text{H}_2}^G)^{n_3} (C_{\text{SLMono}}^S) - k'_{\text{in,HDA}_{\text{Mono}}} (C_{\text{SLNaph}}^S) \quad (21a)$$

$$r_{\text{HDA}_{\text{Naph}}}^L = -r_{\text{HDA}_{\text{Mono}}}^L = -k_{\text{in,HDA}_{\text{Mono}}}^* (p_{\text{H}_2}^G)^{n_3} (C_{\text{SLMono}}^S) + k'_{\text{in,HDA}_{\text{Mono}}} (C_{\text{SLNaph}}^S) \quad (22a)$$

As the solution of this set of equations is quite formidable even for the first-order case, the following simplified set of first-order reaction rate expressions were used to describe the HDA reactions [5,14]:

$$r_{\text{HDA}_{\text{Poly}}}^L = k_{\text{in,HDA}_{\text{Poly}}}^* (p_{\text{H}_2}^G)^{n_1} (C_{\text{SLPoly}}^S) - k'_{\text{in,HDA}_{\text{Poly}}} (C_{\text{SLDi}}^S) \quad (19b)$$

$$r_{\text{HDA}_{\text{Di}}}^L = k_{\text{in,HDA}_{\text{Di}}}^* (p_{\text{H}_2}^G)^{n_2} (C_{\text{SLDi}}^S) - k'_{\text{in,HDA}_{\text{Di}}} (C_{\text{SLMono}}^S) \quad (20b)$$

$$r_{\text{HDA}_{\text{Mono}}}^L = k_{\text{in,HDA}_{\text{Mono}}}^* (p_{\text{H}_2}^G)^{n_3} (C_{\text{SLMono}}^S) - k'_{\text{in,HDA}_{\text{Mono}}} (C_{\text{SLNaph}}^S) \quad (21b)$$

$$r_{\text{HDA}_{\text{Naph}}}^L = -r_{\text{HDA}_{\text{Mono}}}^L = -k_{\text{in,HDA}_{\text{Mono}}}^* (p_{\text{H}_2}^G)^{n_3} (C_{\text{SLMono}}^S) + k'_{\text{in,HDA}_{\text{Mono}}} (C_{\text{SLNaph}}^S) \quad (22b)$$

Because the bench-scale reactor is isobaric and the hydrogen is present in excess, in order to avoid limitations in the concentration of dissolved hydrogen in the liquid phase by the hydrogen solubility, the values of $(p_{\text{H}_2}^G)^{n_1}$, $(p_{\text{H}_2}^G)^{n_2}$, and $(p_{\text{H}_2}^G)^{n_3}$ remain constant; therefore, Eqs. (19b), (20b), (21b), and (22b) are reduced to:

$$r_{\text{HDA}_{\text{Poly}}}^L = k'_{\text{in,HDA}_{\text{Poly}}} (C_{\text{SLPoly}}^S) - k'_{\text{in,HDA}_{\text{Poly}}} (C_{\text{SLDi}}^S) \quad (23)$$

$$r_{\text{HDA}_{\text{Di}}}^L = k'_{\text{in,HDA}_{\text{Di}}} (C_{\text{SLDi}}^S) - k'_{\text{in,HDA}_{\text{Di}}} (C_{\text{SLMono}}^S) \quad (24)$$

$$r_{\text{HDA}_{\text{Mono}}}^L = k'_{\text{in,HDA}_{\text{Mono}}} (C_{\text{SLMono}}^S) - k'_{\text{in,HDA}_{\text{Mono}}} (C_{\text{SLNaph}}^S) \quad (25)$$

$$r_{\text{HDA}_{\text{Naph}}}^L = -k'_{\text{in,HDA}_{\text{Mono}}} (C_{\text{SLMono}}^S) + k'_{\text{in,HDA}_{\text{Mono}}} (C_{\text{SLNaph}}^S) \quad (26)$$

where

$$k'_{\text{in,HDA}_{\text{Poly}}} = k_{\text{in,HDA}_{\text{Poly}}}^* (p_{\text{H}_2}^G)^{n_1} \quad (27)$$

$$k'_{\text{in,HDA}_{\text{Di}}} = k_{\text{in,HDA}_{\text{Di}}}^* (p_{\text{H}_2}^G)^{n_2} \quad (28)$$

$$k'_{\text{in,HDA}_{\text{Mono}}} = k_{\text{in,HDA}_{\text{Mono}}}^* (p_{\text{H}_2}^G)^{n_3} \quad (29)$$

3.6.4. Olefins hydrogenation reaction

The following stoichiometric equation was assumed to represent olefins hydrogenation (HGO):

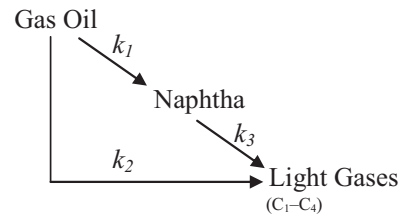
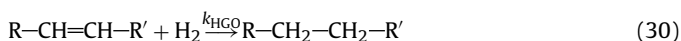


Fig. 1. Reaction scheme of the three-lump kinetic model for mild HCR reactions.

Hydrogenation of olefins was also assumed to be pseudo-first-order with respect to the total concentration of olefins, as given by the following reaction rate equation [14]:

$$r_{\text{HGO}}^L = k'_{\text{in,HGO}} (C_{\text{SLO}}^S) \quad (31)$$

3.6.5. Mild hydrocracking reactions

The mild HCR reactions were simulated using the three-lump model shown in Fig. 1, which includes gas oil, naphtha, and light gases (hydrocarbon gases like C₁–C₄) [14]. The reactions were represented by pseudo-first-order kinetic equations as follows:

$$r_{\text{GO}}^L = \frac{f_w \rho_B r_{\text{GO}}^L}{(\in \mathcal{E}_S)} = k_1 (C_{\text{SLGO}}^S) + k_2 (C_{\text{SLGO}}^S) \quad (32)$$

$$r_{\text{Naphtha}}^L = \frac{f_w \rho_B r_{\text{Naphtha}}^L}{(\in \mathcal{E}_S)} = -k_1 (C_{\text{SLGO}}^S) + k_3 (C_{\text{SLNaphtha}}^S) \quad (33)$$

$$r_{\text{LG}}^L = \frac{f_w \rho_B r_{\text{LG}}^L}{(\in \mathcal{E}_S)} = -k_2 (C_{\text{SLGO}}^S) - k_3 (C_{\text{SLNaphtha}}^S) \quad (34)$$

3.7. Estimation of parameters

3.7.1. Kinetic parameters

Once the reactor equations and assumptions have been established, and HDS, HDN, HDA, and HGO reaction rate expressions have been defined by differential analysis of the experimental data obtained at steady-state conditions [38], the adsorption coefficient, equilibrium constants, reaction orders, frequency factors, and activation energies can be determined by optimization with the Levenberg-Marquardt non-linear regression algorithm [39]. Using the values of parameters obtained from steady-state experiments the dynamic TBR model developed in this work was employed to re-determine the kinetic parameters which were considered as definitive values. The temperature dependencies of all the intrinsic reaction rates constants have been described by the Arrhenius law, which are shown in Table 2.

The dynamic model was considered as a boundary-value problem since the concentration of reactants at the reactor inlet and outlet are known. Therefore, to solve the two-point boundary-value problem, it was employed the “shooting method” to determine the apparent reaction rate constants [14]. The shooting method reduces the solution of a boundary-value problem to the iterative solution of an initial-value problem. In general, this method consists of a trial-and-error procedure in which a boundary point having the best-known conditions is selected as the initial point. Any other missing initial conditions are assumed. The initial-value problem is then solved using the fourth-order Runge-Kutta algorithm. Unless the computed solution agrees with the known boundary conditions (unlikely on the first trial), the initial conditions are adjusted and the problem is solved again. For each experiment, this process is repeated until the calculated solution agrees with the known boundary conditions within specified tolerances given by the following non-negative objective function [40]:

$$F = \left| (C_i^L)_{L_B, \text{calc}} - (C_i^L)_{L_B, \text{exp}} \right| \quad (35)$$

Table 2

Kinetic and hydrodynamic parameters for gas oil HDT reactions.

Reaction <i>j</i>	$k_{0,j}^a$	$E_{a,j}$ (kJ/mol _i)	$K_{0,ij}^b$	$\Delta H_{ads,i}$ (kJ/mol _i)	$\Delta H_{R,j}^L$ (kJ/mol H ₂)
HDS ^c	2.639287×10^{17}	150.10	5.166888	34.02	34.89 ^d
HDN	1.553296×10^{12}	172.28	–	–	21.62 ^e
HDA _{Poly}	2.413720×10^{10}	156.09	9.856780	–	58.61 ^f
HDA _{Di}	2.855135×10^8	131.91	66.570899	–	58.61 ^f
HDA _{Mono}	11.143786	54.31	438.006631	–	58.61 ^f
HGO	9.463471×10^8	138.15	–	–	101.10 ^g
HCR _{GO-Naphtha}	1.384870×10^{-1}	56.41	–	–	29.31 ^f
HCR _{GO-LG}	2.391640×10^6	139.46	–	–	29.31 ^f
HCR _{Naphtha-LG}	2.212240×10^{16}	273.78	–	–	29.31 ^f
Temperature (°C)	A'	b'			
340	0.0401397	1.5552485			
350	0.1759018	0.8613340			
360	0.1963370	0.6933859			
370	1.0277×10^{-3}	2.2143412			
380	1.9970×10^{-4}	2.5912252			

^a See nomenclature for units of HDS reaction, k_0 [=] cm³/L/(g_S s) for HDA and HGO reactions, and k_0 [=] 1/s for HDN and mild HCR reactions.^b For HDS reaction i = H₂S and its units are cm³/mol_{H₂S}, for HDA reactions $K_{0,ij}$ is at T_0 = 340 °C and dimensionless.^c m_1 = 1.8, m_2 = 0.96.^d From ref. [56].^e From ref. [47].^f From ref. [36].^g From ref. [23].

The HDS reaction rate was taken according to the kinetic model given by Eq. (12) with m_1 = 1.8 and m_2 = 0.96.

For HDA reactions, in order to determine the backward reaction rate constants, the equilibrium constants were defined as follows:

$$K_{HDA_{Poly}} = \frac{k'_{in,HDA_{Poly}}}{k'_{in,HDA_{Poly-}}} \quad (36)$$

$$K_{HDA_{Di}} = \frac{k'_{in,HDA_{Di}}}{k'_{in,HDA_{Di-}}} \quad (37)$$

$$K_{HDA_{Mono}} = \frac{k'_{in,HDA_{Mono}}}{k'_{in,HDA_{Mono-}}} \quad (38)$$

The equilibrium constants for reversible reactions were evaluated at different temperatures by using the van't Hoff equation:

$$K_{HDA_{Poly/Di/Mono}} = K_{0,HDA_{Poly/Di/Mono}}(T_0) \times \exp \left[\frac{-\Delta H_{R,HDA_{Poly/Di/Mono}}^L}{R} \left(\frac{1}{T_0} - \frac{1}{T_S} \right) \right] \quad (39)$$

Aromatic hydrogenation reactions are exothermic with heats of reaction between 63 and 71 kJ/mol H₂ [5,14,35,36,41]. Therefore, the heat of reaction for HDA was assumed to be the average value of 67 kJ/mol of reacted H₂. The kinetic parameters for the hydrogenation of poly-, di-, and monoaromatics are given in Table 2.

The ODEs representing the mild HCR reactions according to the scheme given in Fig. 1 are:

$$\frac{dY_{GO}}{d(1/LHSV)} = -(k_1 + k_2)Y_{GO} \quad (40)$$

$$\frac{dY_{Naphtha}}{d(1/LHSV)} = k_1Y_{GO} - k_3Y_{Naphtha} \quad (41)$$

$$\frac{dY_{LG}}{d(1/LHSV)} = k_2Y_{GO} + k_3Y_{Naphtha} \quad (42)$$

The HCR reaction rate constants were estimated by minimizing the difference between the experimental and predicted values of

product yields. The objective function to estimate these parameters was defined as follows:

$$F = \sum_{k=1}^{N_{exp}} \sum_{i=1}^{N_{lump}} (Y_{i,exp} - Y_{i,calc})_k^2 \quad (43a)$$

where

$$\sum_{i=1}^{N_{lump}} Y_{i,calc} = 1 \quad (43b)$$

This function was solved using the Matlab commercial software with the Levenberg-Marquardt's optimization procedure [42]. The estimated HCR kinetic parameters values are shown in Table 2.

3.7.2. Catalyst effectiveness factor

The catalyst effectiveness factor can be estimated as function of the Thiele modulus (Φ). The generalized Thiele modulus for n th-order irreversible reaction is [43]:

$$\Phi_j^L = \frac{1}{\phi_S} \left(\frac{V_p}{S_p} \right) \sqrt{\left(\frac{n+1}{2} \right) \frac{\rho_S k'_{in,j} (C_{SLi}^S)^{n-1}}{D_{ei}^L}} \quad (44)$$

For n th-order reversible reaction, the generalized Thiele modulus is

$$\Phi_j^L = \frac{1}{\phi_S} \left(\frac{V_p}{S_p} \right) \sqrt{\left(\frac{n+1}{2} \right) \frac{\rho_S k'_{in,j} (C_{SLi}^S)^{n-1}}{D_{ei}^L} \frac{(K_j + 1)}{K_j}} \quad (45)$$

where

$$D_{ei}^L = \frac{\epsilon_S}{\tau} \left[\frac{1}{(1/D_{Mi}^L) + (1/D_{Ki}^L)} \right] \quad (46)$$

$$\epsilon_S = \rho_S V_g \quad (47)$$

$$\rho_S = \frac{\rho_B}{(1 - \epsilon_B)} \quad (48)$$

The equivalent particle diameter (d_{pe}) was estimated using the following expression proposed by Cooper et al. [44]:

$$d_{pe} = \frac{6(V_p/S_p)}{\phi_S} \quad (49)$$

The tortuosity factor (τ) generally has a value of 2–7. Usually, tortuosity factor is assumed to be 4 according to the literature reports [45]. According to Satterfield [46], Knudsen diffusion is not observed in liquids, therefore $D_{Ki}^L = 0$.

The following equations are employed for determining the values of η for each reaction [10,43,47]:

- for $\Phi_j^L < 3$

$$\eta_j^L = \frac{\tanh(\Phi_j^L)}{\Phi_j^L} \quad (50)$$

- for $\Phi_j^L \geq 3$

$$\eta_j^L = \frac{1}{\Phi_j^L} \quad (51)$$

3.7.3. Hydrodynamic parameters

According to Satterfield [48] the catalyst wetting efficiency is defined with the following ratio:

$$f_w = \frac{k'_{app,HDS}}{k'_{in,HDS}} \quad (52)$$

The catalyst wetting efficiency in experimental reactors has been reported to be in the range of 0.12–0.6, while for commercial reactors in the range of 0.7–1.0 [14,48].

In the present work, the following partial wetting model of Bondi [49] modified by Satterfield [48], was used to correlate the apparent rate constant, $k'_{app,HDS}$, with the superficial liquid mass velocity, G_{mL} , and the intrinsic rate constant, $k'_{in,HDS}$:

$$k'_{app,HDS} = \frac{1 \times 10^5}{(1/k'_{in,HDS} \times 10^{-5}) + (A'/(G_{mL})^{b'})} \quad (53)$$

The f_w - Re_L curve given by this correlation must be obtained by varying the liquid mass velocity for only one reactor temperature. The values of the empirical constants A' and b' for different temperatures are given in Table 2. The intrinsic reaction rate constant ($k'_{in,HDS}$) is a temperature function that may be further developed into the Arrhenius equation:

$$k'_{in,HDS} = k'_{0,HDS} \exp\left(\frac{-E_{a,HDS}}{RT_S^S}\right) \quad (54)$$

The model makes use of correlations reported in the open literature in order to calculate transport and thermophysical properties [50].

4. Results and discussion

The three-phase isothermal reactor model developed in this work was applied to analyze and simulate the performance of a bench-scale reactor. The model solution for the experimental reactor is an initial-value problem as the concentrations of reactants and products are known at the reactor inlet. The model was solved with the kinetic parameters estimated from experiments as reported previously.

The calculation of the initial molar concentrations for sulfur-, nitrogen-containing compounds and olefins can be made by the following expressions:

$$(C_S^L)_0 = \frac{(\rho_L)_0}{32.066} (w_S)_0 \quad (55)$$

$$(C_N^L)_0 = \frac{(\rho_L)_0}{14.00674} (w_N)_0 \quad (56)$$

$$(C_O^L)_0 = \frac{(\rho_L)_0}{247.06} (w_O)_0 \quad (57)$$

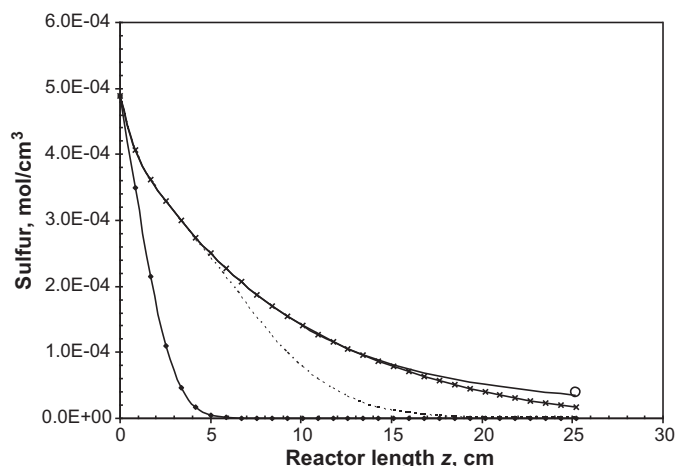


Fig. 2. Sulfur concentration along the catalyst bed length in the bench-scale trickle-bed reactor at different times. (♦) 60 s, (···) 400 s, (×) 900 s, (–) 1700 s, (○) experimental value.

For the remaining organic compounds it was assumed that they have the same molecular weight as the whole sample, so that it is possible to use their weight fractions to calculate concentrations:

$$(C_i^L)_0 = \frac{(\rho_L)_0}{MW_L} (w_i)_0 \quad (58)$$

where i = Poly, Di, Mono, Naph, GO, and Naphtha. The estimation of the final weight fractions is done with:

$$(w_i)_f = \frac{MW_L}{(\rho_L)_f} (C_i^L)_f \quad (59)$$

The initial liquid concentration of the gaseous compounds is estimated with the following expression:

$$(C_i^L)_0 = \frac{(p_i^G)_0}{H_i} \quad (60)$$

where i = H_2 , H_2S , NH_3 , and CH_4 . Methane was taken as the representative compound for light hydrocarbons (C_1 – C_4) kinetics.

4.1. Dynamic simulation of an isothermal HDT bench-scale reactor

Simulation results of the bench-scale reactor are based on the experimental operating conditions and parameters given earlier. The kinetic parameters estimated above by minimizing the differences between model predictions and experimental results, were used to simulate the behavior of the bench-scale TBR.

The variation of the sulfur concentrations in the liquid phase along the length of the catalyst bed is presented in Fig. 2. The concentration profiles at different times were generated at a reactor temperature of 340 °C, pressure of 5.3 MPa, LHSV of 2.5 h^{−1}, and H_2 /oil ratio of 356 std m³/m³ (2000 scf/bbl). The experimental sulfur content at the exit of the reactor is well predicted. At short time (i.e., 60 s) the feed only reaches 20% of the total reactor length, that is why the sulfur content in the remaining 80% of the reactor length is zero, which means that this part of the reactor is empty. As the time passes the reactor is completely filled with the reacting mixture, reaching the steady-state condition at 1700 s. The variation of the hydrogen partial pressure in the gaseous phase and the concentration in the liquid phase along the catalyst bed length are shown in Fig. 3. It has been established by steady-state simulations that the curve shape of hydrogen concentration in the liquid phase is dictated by a balance between mass transfer and reaction rate. This is much clearly observed from dynamic simulation results.

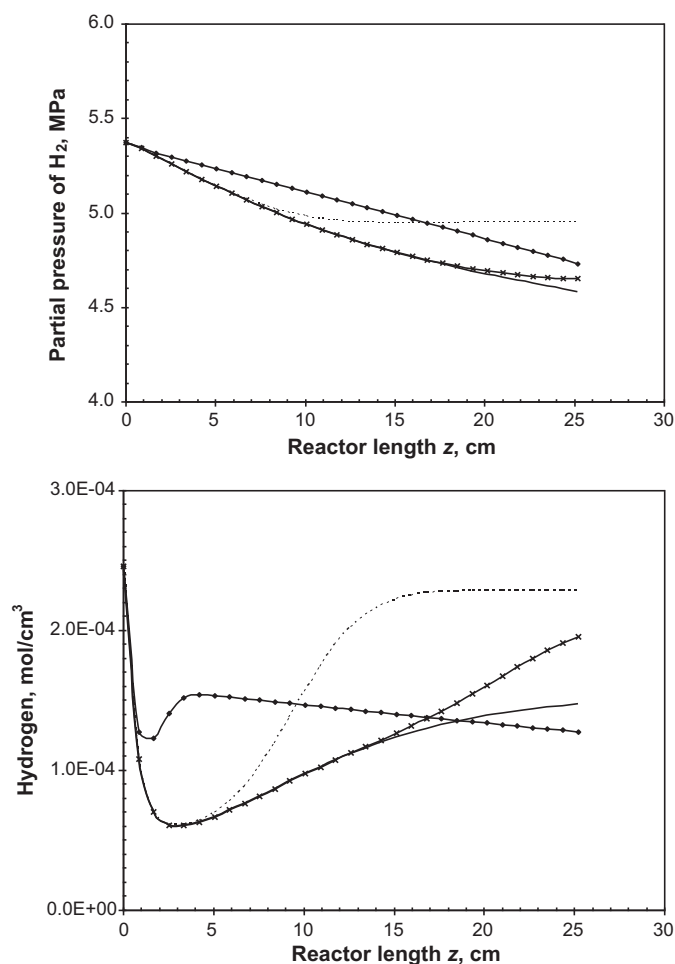


Fig. 3. H_2 partial pressure and liquid molar concentration along the catalyst bed length in the bench-scale trickle-bed reactor at different times. (♦) 60 s, (···) 400 s, (×) 900 s, (—) 1700 s.

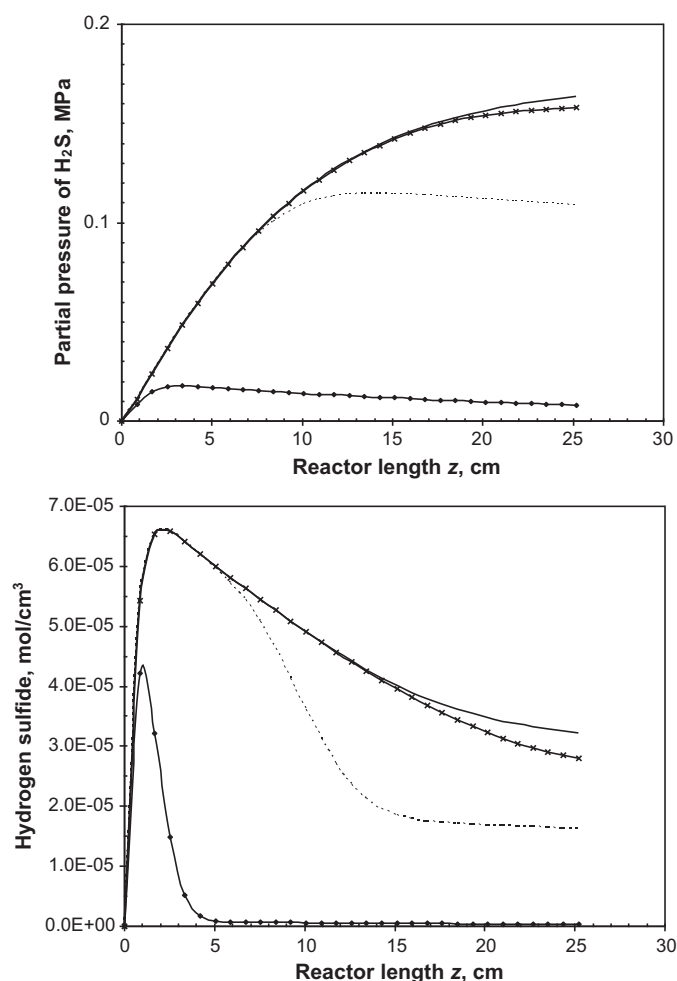


Fig. 4. H_2S partial pressure and liquid molar concentration along the catalyst bed length in the bench-scale trickle-bed reactor at different times. (♦) 60 s, (···) 400 s, (×) 900 s, (—) 1700 s.

The variation of H_2S partial pressure in the gaseous phase and its concentration in the liquid phase along the catalyst bed length are shown in Fig. 4. Similarly to H_2 partial pressure and concentration in the liquid phase, H_2S profiles follow the well-known tendencies. Since H_2S is not present at the inlet of the reactor as the time passes, its partial pressure and concentration are increased. At short times, H_2S is produced until certain length of the reactor because sulfur is present and reacts with H_2 . After that point there is no more reacting mixture and the reaction stops.

The simulation results at steady-state (1700 s) were compared with experimental measurements for HDS. The developed model was found to simulate the performance of the bench-scale TBR with high accuracy, obtaining errors in sulfur conversion prediction ranging from -1.13% to $+0.56\%$.

Once the model was found to properly represent the experimental data it was applied to simulate the performance of the bench-scale reactor at operating conditions different from those used to determine the kinetic parameters. The effect of pressure on HDS at steady-state is presented in Fig. 5. As expected, the product sulfur content was found to decrease with increasing the pressure. At higher operating pressure, the concentration of hydrogen in diesel oil increases because of the increased solubility of hydrogen. That favors the removal of impurities. However, at highest pressure and lowest LHSV there is not much difference between sulfur conversions, since most of this impurity (and others) has been removed.

Fig. 6 shows the effect of reactor temperature on the hydrogenation of aromatics and compares the simulation results with experimental measurements. The model output was found to agree reasonably well with the experimental data. The conversion of polyaromatics reached a maximum at a reactor temperature of $360^\circ C$.

At high temperature the differences between experimental and simulated results for poly- and diaromatics are more notorious,

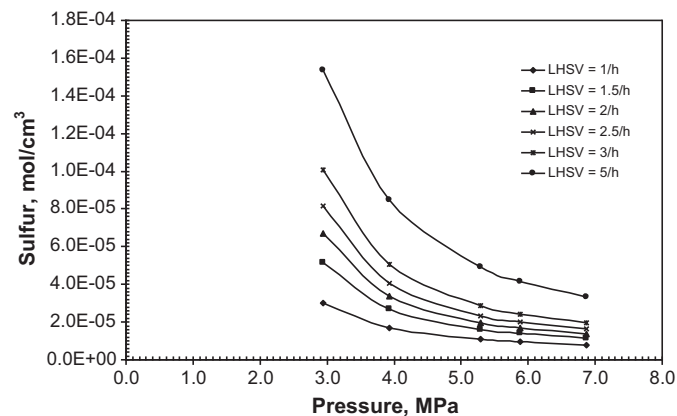


Fig. 5. Simulation of bench-scale reactor at steady-state: Effect of pressure ($T = 350^\circ C$).

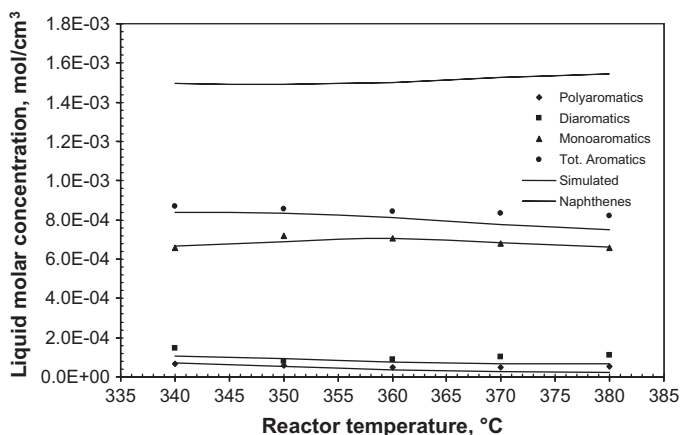


Fig. 6. Effect of reactor temperature on hydrogenation of aromatics (at steady-state).

which may be explained by the following reasons [5,17]: (i) as temperature is increased there is higher removal of sulfur and nitrogen compounds thus increasing the yield of H_2S and NH_3 , which are reported to inhibit the HDA reactions, and this effect is not taken into account in the power-law kinetic models used, and (ii) the consideration of tri-, tetra-, and penta-aromatics as a single group of polyaromatic compounds. To overcome this problem, Melis et al. [17] developed a model based on a detailed lumped scheme for the hydrogenation reactions, which accounts for ten different aromatic classes and assumes that HDA reactions occur according to the LHHW kinetics. Unfortunately, the use of this model was not possible in this work due to the limitations of the analytical methods applied.

The production or negative conversions obtained for monoaromatic compounds ($(C_{Mono}^L)_f > (C_{Mono}^L)_0 \cong 5.8 \times 10^{-4} \text{ mol/cm}^3$), are justified because they depend on the rates at which the reactions from poly- to diaromatics, from di- to monoaromatics, and from monoaromatics to naphthenes proceed. Cooper et al. [41,44] and Chowdhury et al. [5] have also reported negative conversions for di- and monoaromatics. The conversion of monoaromatics was lower than those for poly- and diaromatics. At constant LHSV of 2.5 h^{-1} , the conversion was found to decrease up to 350°C and then increased. This can be explained by the faster rate of diaromatics hydrogenation, producing monoaromatics, compared with the rate of monoaromatics hydrogenation. The conversion of monoaromatics, as expected, was more difficult under the operating conditions studied in this work.

Polyaromatics are hydrogenated to a considerable extent at 360°C , while at this temperature monoaromatics start reacting. However, the increase of temperature on polyaromatics hydrogenation was insignificant.

Since remarkable conversion of di- and polyaromatic compounds to monoaromatics can occur with little or no change in the total aromatic content, it is necessary when evaluating catalyst and process performance to use methods that measure the concentration of the different aromatic species, at least as poly-, di-, and monoaromatic compounds.

The degree of poly- and diaromatics hydrogenation goes through a maximum as the reaction temperature is increased; that is, the poly- and diaromatics hydrogenation decreases as the temperature is further raised, which means that at higher temperatures those reactions are under thermodynamic equilibrium limitation. At lower temperature, monoaromatics hydrogenation reaction is controlled by thermodynamic equilibrium, while at higher temperatures, the reaction is kinetically controlled. Conversion of di- and polyaromatics to monoaromatics occurs even at low severities (low

temperatures and high LHSVs), but monoaromatics remain nearly unchanged and even their content in the product can be higher than that originally present in the feed. This is not unexpected since every mole of polyaromatic compound that is saturated would add a mole to the diaromatics, and every mole of diaromatic compound hydrogenated would add a mole to the monoaromatic category, which is hydrogenated at a slower rate than the corresponding diaromatic compound.

Thus hydrogenation of the monoaromatics is the key step in the production of low-aromatic diesel fuel, and therefore, an acceptable total aromatics reduction can only be achieved at severe operating conditions such as high temperature, low LHSV, and high pressure.

The model was also applied to simulate the performance of the bench-scale reactor for HDN, HGO, and mild HCR reactions. The yields of light gases and naphtha were found to increase with increasing reactor temperature. The simulation results for these reactions agreed well with the experimental data.

4.2. Dynamic simulation of an isobaric nonisothermal HDT industrial reactor

The three-phase nonisothermal reactor model was used to simulate the performance of the industrial reactor. The model solution for the commercial reactor becomes also an initial-value problem because the concentrations of reactants and products and initial temperature of phases are known at the reactor inlet. The model was solved with the rate constants estimated from the experiments in the bench-scale reactor. The wetting efficiency (f_w) was assumed to be 1.0 taking into account the high liquid velocities present in industrial reactors [11,48].

Fig. 7 illustrates the dynamic profiles of sulfur concentration and temperature of industrial HDT reactor which were calculated with mass and energy balance equations (Eqs. (1)–(6)). The result of the transient simulation of sulfur profiles of bench-scale reactor and experimental temperature are also shown for comparison (dotted lines). It can be observed that the steady-state was reached at the same time (1700 s), which is due to the same space velocity and initial temperature used in both reactors. Because single point at steady-state is used to validate the dynamic model some uncertainty remains regarding the shape of dynamic profiles of bench-scale and industrial reactor. According to Carberry and Varma [51], the small peak in the sulfur concentration profile at the outlet of the commercial reactor is a typical response from HDT reactors that performs well with a weak bypass effect.

Fig. 7 also shows the dynamic temperature simulation for the commercial reactor. The phenomenon called “wrong-way” behavior was not encountered at the beginning of the reactor as reported for other cases [28]. This can be attributed to the fast and high conversion of reactants in the first 25% of the catalyst bed, in such a way that there is not enough reactant in the remaining length of the reactor that leads to a transient temperature diminution.

Fig. 8 shows the predicted dynamic liquid molar concentration profiles of sulfur along the commercial catalytic bed at different times ranging from 60 to 1700 s for an inlet reactor temperature of 340°C . The dynamic simulation was carried out at the same reaction conditions than those employed for the simulation of the bench-scale reactor. The value of sulfur concentration reported at the exit of the isothermal bench-scale reactor is included in this figure (symbol “○”).

The profiles presented in Fig. 8 with a pronounced reduction of sulfur concentration on the first section of the reactor, have been already reported by Jiménez et al. [52]. They attributed those sulfur concentration shapes in the catalytic bed to the kinetic model considered and to the operating conditions simulated. Also, the bench-scale experimental sulfur concentration value was higher than that predicted for the industrial reactor because of the

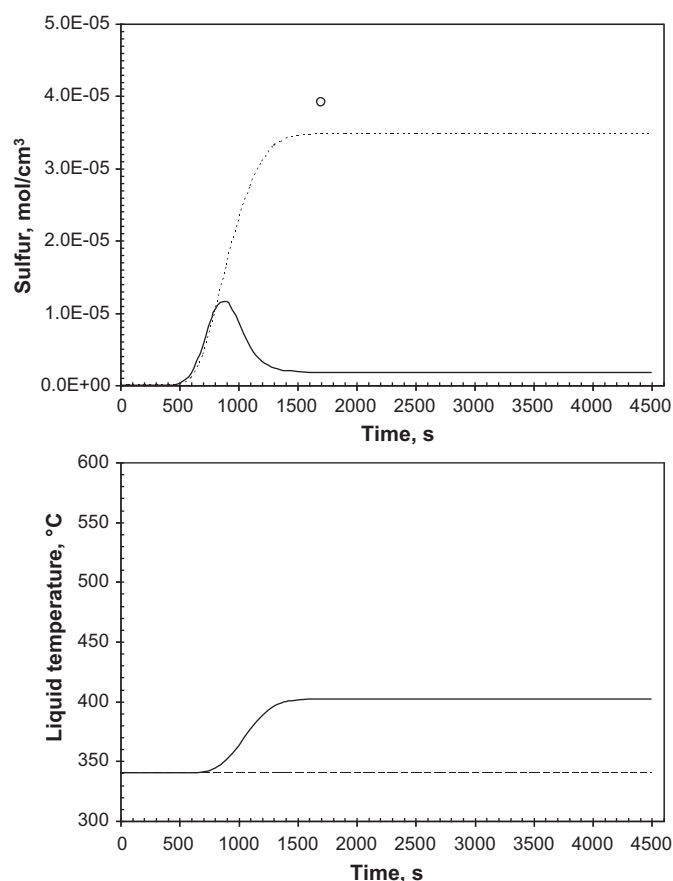


Fig. 7. Profiles of (—) sulfur concentration and temperature on commercial reactor, (○) experimental sulfur concentration at the outlet of catalyst bed, (---) dynamic sulfur concentration in experimental reactor, (---) experimental isothermal temperature (Commercial reactor, 340 °C; 5.3 MPa; $z=853.44$ cm; $u_L=0.72$ cm/s; $u_G=8.93$ cm/s. Bench-scale reactor, 340 °C; 5.3 MPa; $z=25.2$ cm; $u_L=1.81 \times 10^{-2}$ cm/s; $u_G=0.24$ cm/s).

increasing catalytic bed temperature observed in the liquid phase of the adiabatic reactor.

Fig. 9 reports the predicted evolution of temperature of the liquid phase along the industrial reactor at different times. In this figure the catalyst (or solid phase) temperature profile is not shown,

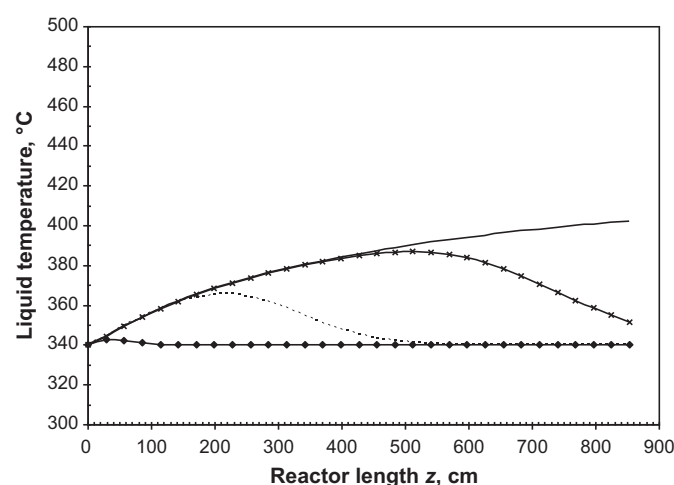


Fig. 9. Simulated temperature profiles of the liquid phase down through the catalyst bed of commercial reactor with time. (♦) 60 s, (···) 400 s, (×) 900 s, (—) 1700 s.

because the difference of temperature between the liquid and catalyst was of only 0.03 °C. This result validates the simulation of the heat balance with only one equation for a pseudo-phase, as it was reported elsewhere [28]. This figure also demonstrates that the increase in reaction temperature is higher in the initial part of the reactor, due to the greater removal of impurities that occurs in this zone, which has been also reported by others [18].

The transient behavior of the sulfur concentration in the commercial HDT reactor is illustrated in Fig. 10. It can be observed that there is a distinctive maximum in transient values, which is highest at the top of the reactor and progressively decreases down the reactor. Those transient sulfur concentration profiles together with the concentration profiles of the other compounds shown in Fig. 11, are important for on-line tuning of the controllers settings in the control system of hydrotreating processes [23,25].

Fig. 12 shows the predicted concentration profiles at steady-state of the main compounds in liquid phase along the commercial reactor: sulfur, nitrogen, poly-, di-, monoaromatics, naphthenes, and olefins. From this figure it is possible to observe that the feed containing several types of mono-, di-, and condensed polyaromatic structures, exhibits hydrogenation reactivities considerably different. Since more moles of H_2 are involved in the final ring hydrogenation (3 mol for monoaromatics compared with 1 or

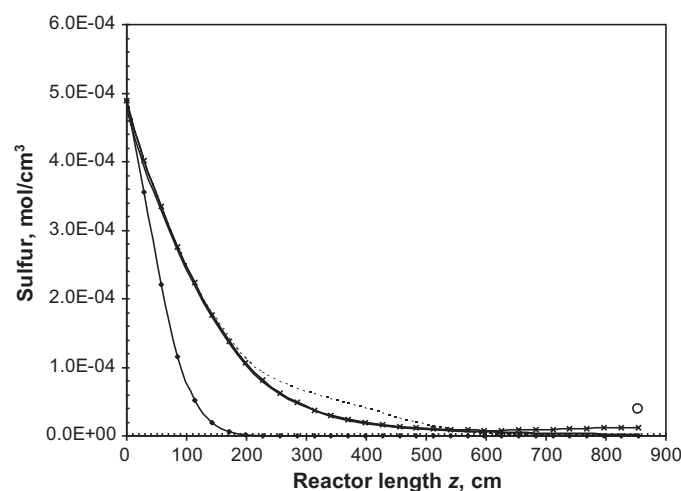


Fig. 8. Concentration profiles of sulfur down through the catalyst bed of the commercial reactor with time. (○) Experimental bench-scale value, (lines) predicted values for commercial reactor. (♦) 60 s, (···) 400 s, (×) 900 s, and (—) 1700 s.

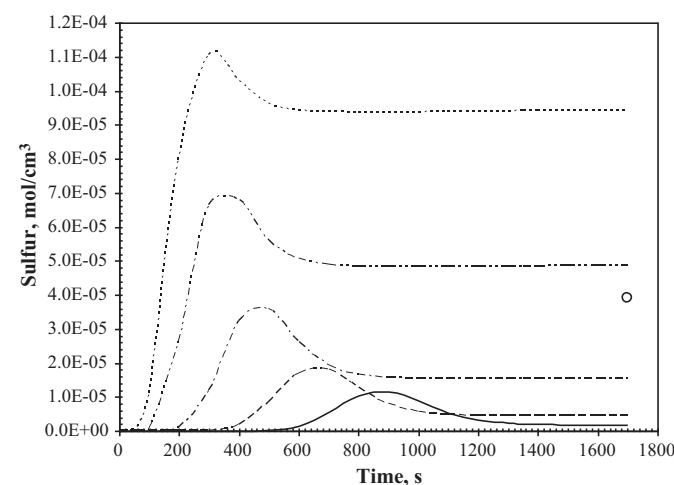


Fig. 10. Dynamic sulfur concentration profiles in the liquid phase of commercial reactor. (···) $z=213.4$ cm, (— · — · —) $z=284.5$ cm, (— · — · —) $z=426.7$ cm, (---) $z=640.1$ cm, (—) $z=853.4$ cm, and (○) experimental bench-scale value.

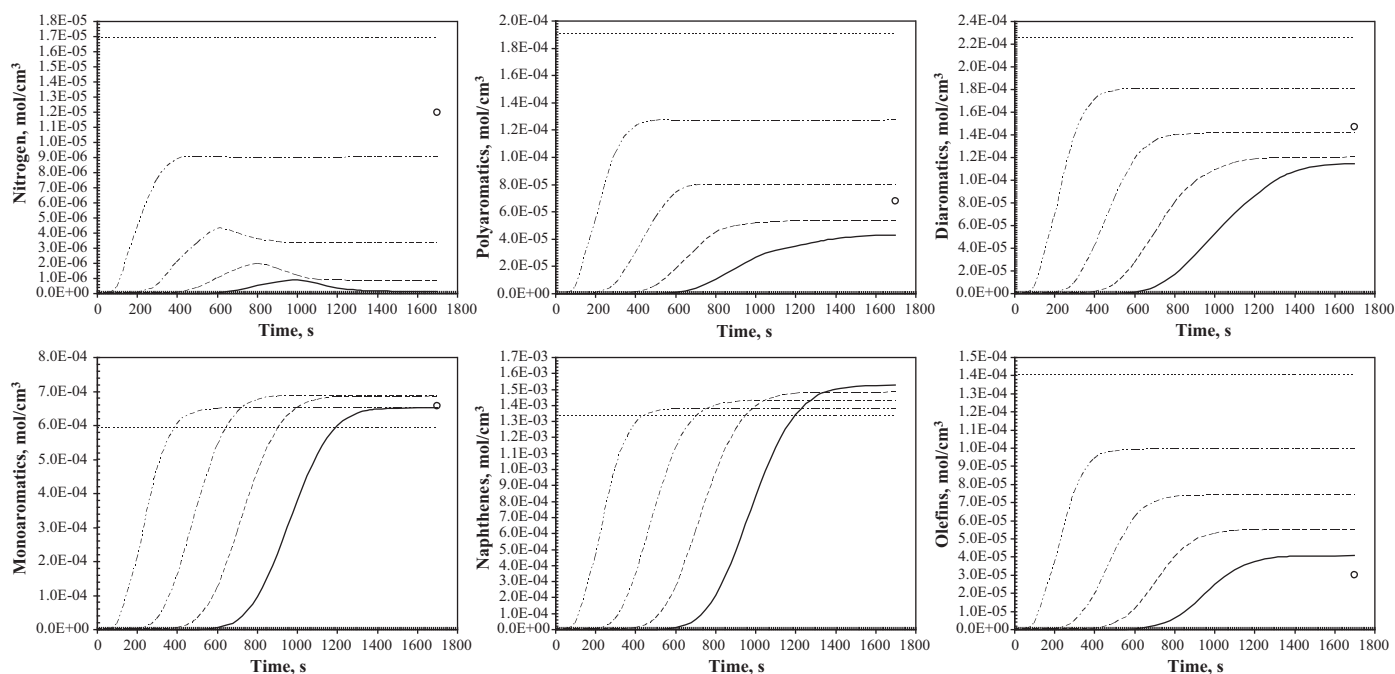


Fig. 11. Dynamic nitrogen, polyaromatics, diaromatics, monoaromatics, naphthenes, and olefins concentration profiles in the liquid phase of commercial reactor. (...) $z = 0$ cm, (---) $z = 213.4$ cm, (---) $z = 426.7$ cm, (---) $z = 640.1$ cm, (—) $z = 853.4$ cm, and (○) experimental bench-scale value.

2 mol for hydrogenation of poly- or diaromatics, respectively), hydrogenation of the first ring in polyaromatics is usually less thermodynamically favored (with lower equilibrium constant values) than hydrogenation of the final ring of the monoaromatics at typical HDT conditions. On the other hand, it has also been observed the first-ring hydrogenation of polyaromatics to be most favored kinetically. The hydrogenation rates of subsequent rings tend to become lower (see Table 2), and hydrogenation of the last ring (corresponding to monoaromatics) proceeds with considerable difficulty compared with the initial hydrogenation steps [35]. For this study, monoaromatics hydrogenation was limited by thermodynamic equilibrium, which favors the reverse reaction, as the monoaromatics concentration increased along the catalytic bed instead of decreasing. It means that the diaromatics to monoaromatics forward reaction was much faster than the monoaromatics to naphthenes forward reaction, and the reduction of total aromatics is therefore small.

The variations in gas oil and naphtha dynamic concentration within the commercial reactor are shown in Fig. 13. The concentration profiles of liquid compounds involved in mild HCR reactions in the catalyst bed at steady-state are also given in Fig. 13.

Due to the lower acidity of the carrier (γ - Al_2O_3), the commercial CoMo catalyst used in our experiments produces a low yield of naphtha by HCR. From Table 2, it is observed, according to pre-exponential factor values, that HCR of gas oil to naphtha is not as easy as HCR of gas oil to light gases. This is because breaking side chains of one to four carbons to produce light gases is easier than breaking long chains with more carbons into naphtha.

The transient variation of hydrogen, hydrogen sulfide, and ammonia partial pressures in the gaseous phase at different bed locations are shown in Fig. 14. In general, hydrogen partial pressure decreases along the reactor as a result of H_2 consumption and increase in solubility, while hydrogen sulfide and ammonia partial pressures have the opposite behavior due to sulfur and nitrogen removals, respectively. Methane partial pressure profiles were omitted because its yield by mild HCR reactions was negligible.

Partial pressure profiles of the main gaseous compounds in the simulated commercial HDT reactor at steady-state are presented in Fig. 15. This figure illustrates the predicted steady-state partial pressures of H_2 , H_2S , NH_3 , and CH_4 in the gas phase along the axial position of the reactor. It can be seen that the H_2 partial pressure in the gas phase decreases gradually, while the partial pressure of H_2S in the gas phase increases along the reactor as HDS is occurring. According to Melis [17], the practically constant H_2 partial pressure along the reactor means that HDT reaction was conducted under H_2 excess. The partial pressure of CH_4 presents a limited increase along the catalytic bed due to the beginning of the mild HCR reactions (mainly formed by cracking of the alkyl groups), as reactor temperature also increased along the reactor. The production of NH_3 by HDN reaction is negligible compared with H_2S formed from HDS reaction, which could be explained by the low conversion of nitrogen compounds observed in Fig. 12.

The temperature profiles in the commercial reactor for various positions in the axial direction are given in Fig. 16. These profiles

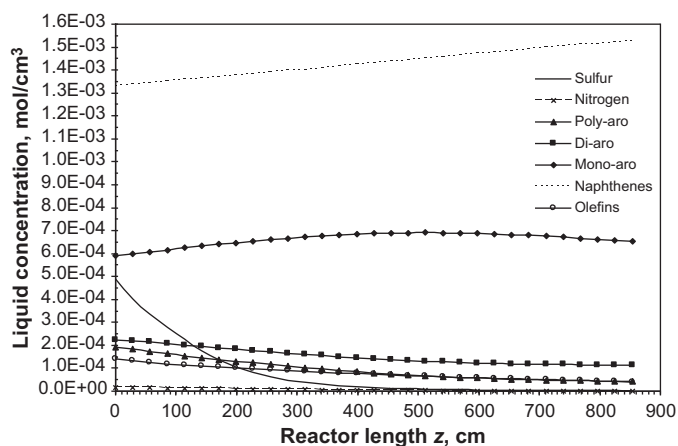


Fig. 12. Simulated concentration profiles of liquid compounds along the commercial reactor length at steady-state.

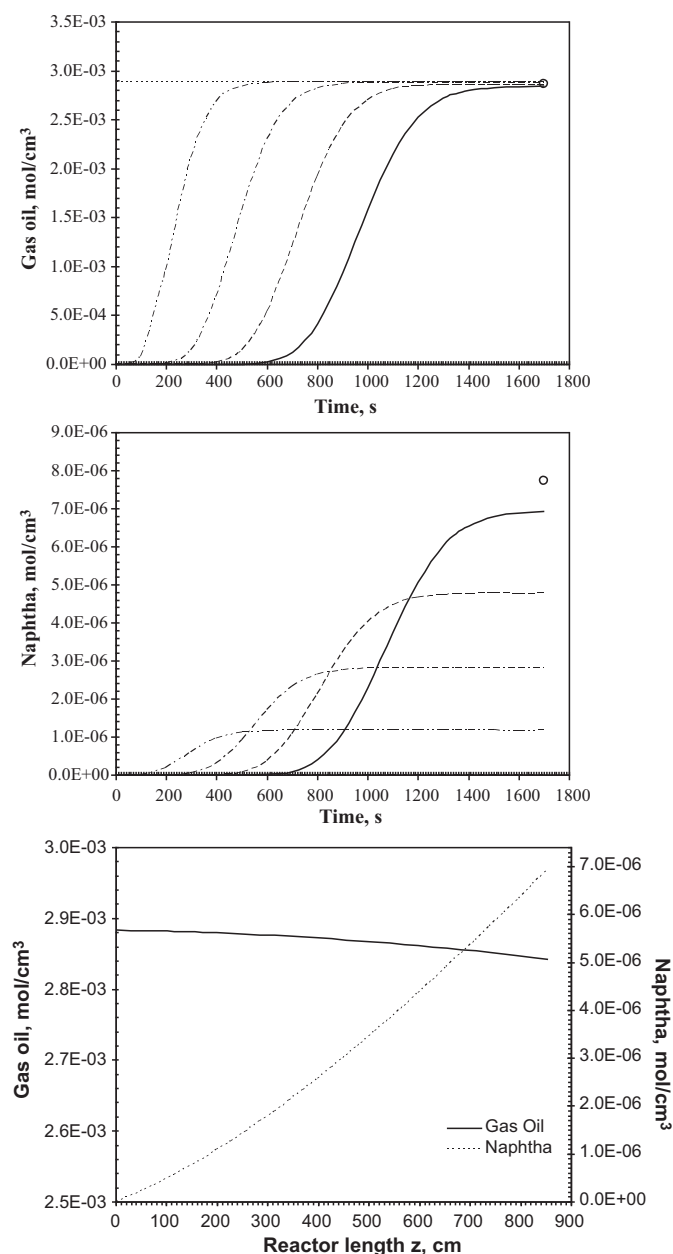


Fig. 13. Dynamic gas oil and naphtha concentration profiles in the liquid phase of commercial reactor and at steady-state along commercial catalyst bed. (···) $z = 0$ cm, (·····) $z = 213.4$ cm, (— · — ·) $z = 426.7$ cm, (---) $z = 640.1$ cm, (—) $z = 853.4$ cm, and (○) experimental bench-scale value.

show the simulated change in liquid phase temperature with time, starting from an initial temperature in the catalyst bed of 340°C , over a time period of about 1700 s. In the axial direction, there are strong temperature gradients. However, the temperature profiles show a fairly smooth distribution in z -direction.

In order to simulate the effect of commercial size catalyst particles, the effectiveness factors were estimated based on chemical structures of the reactant compounds and arrived from correlations given earlier. The intraparticle diffusion limitations are reflected in the values at steady-state of the catalyst effectiveness factors listed in Table 3. The reactants with more than one benzene ring have lower value due to their higher resistance to pore diffusion [53]. At commercial scale, the temperature increases along the HDS reactor due to adiabatic mode of operation and the exothermic nature of reaction. The constant rate of reaction is then increased as function of reactor length and thus an increase of Thiele modulus can be

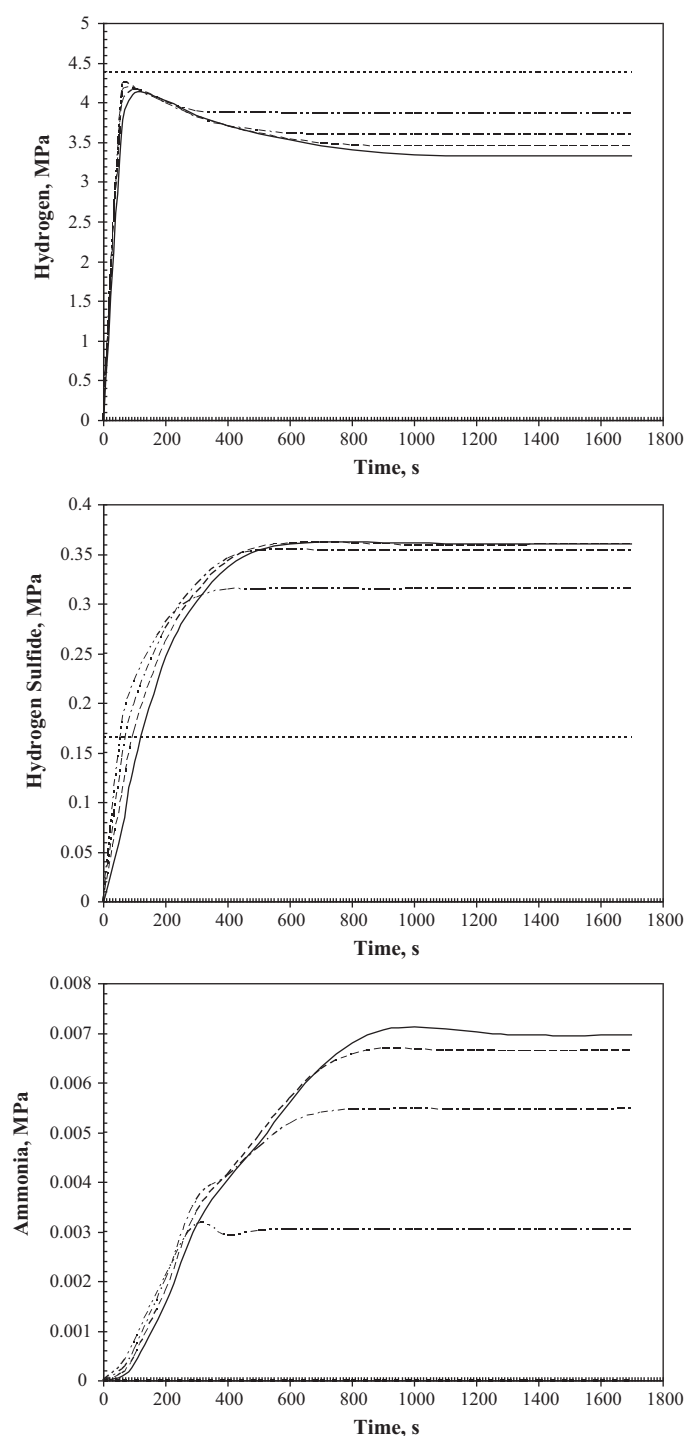


Fig. 14. Dynamic H_2 , H_2S , and NH_3 partial pressure profiles in the commercial reactor. (···) $z = 0$ cm, (·····) $z = 213.4$ cm, (— · — ·) $z = 426.7$ cm, (---) $z = 640.1$ cm, (—) $z = 853.4$ cm, and (○) experimental bench-scale value.

expected. On the other hand at the reactor entrance the sulfur concentration at solid surface is high. The combination of these facts causes the effectiveness factor to be low with a tendency to increase as the mixture passes through the reactor because the sulfur concentration at solid surface diminishes rapidly (see Fig. 8), and the diffusivity coefficient is increased because of increased temperature. Similar dependency of effectiveness factor on position was reported by Froment et al. [7]. The other reactions show different behavior with respect to changes in effectiveness factors as function of reactor length, i.e. either decrease or remain constant, which

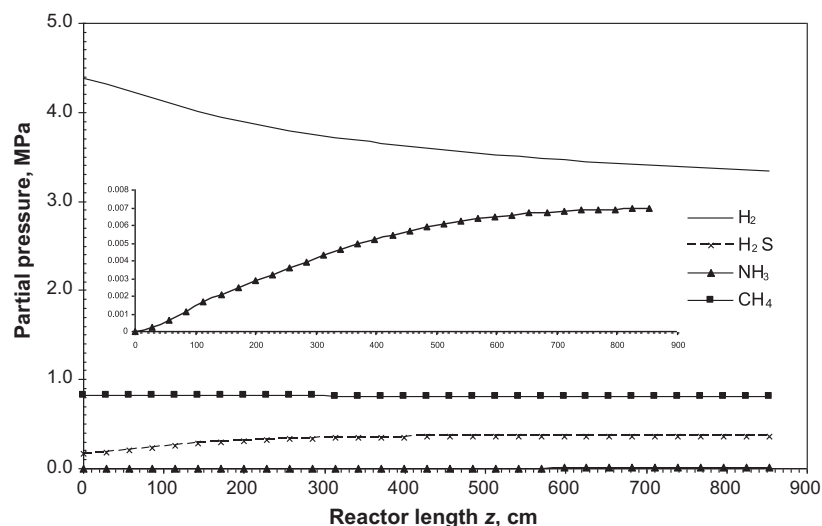


Fig. 15. Simulated partial pressure profiles of gaseous compounds along the commercial reactor at steady-state.

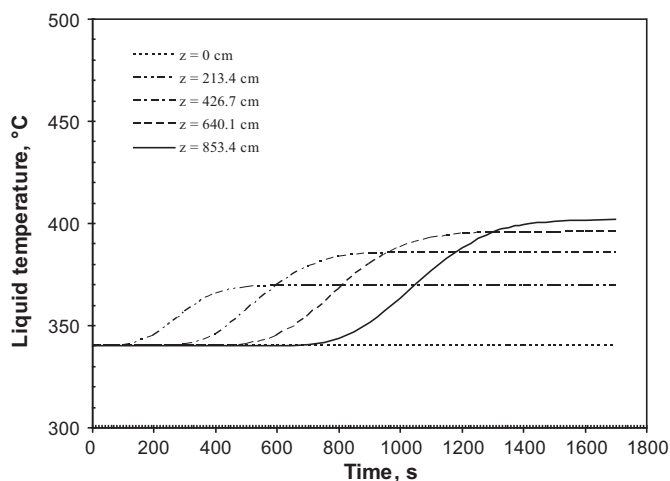


Fig. 16. Transient temperature profiles in the commercial reactor at different bed positions.

is mainly due to the consideration of first order of reaction, and thus independency of Thiele modulus on concentration of species [54]. Therefore, the prevailing effect is the rate constant, provoking decreased effectiveness factor for those positions far from reactor entrance.

Fig. 17 shows the transient behavior of the effectiveness factor for HDS reaction, assuming a typical reaction order of 1.7, at different positions in the catalyst bed.

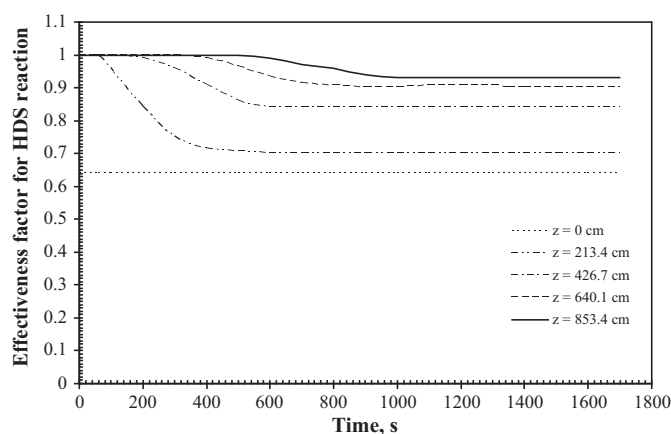


Fig. 17. Transient effectiveness factor for HDS reaction in the commercial reactor at different bed positions.

When the concentration of limiting reactant within pores becomes less by chemical reaction along the catalyst bed, the rate of diffusion becomes higher than the reaction rate and then the effectiveness factor value increases along the catalyst bed. Fig. 17 shows that steady-state inside the catalyst pores was achieved faster than in the liquid phase, which justifies to approximate the catalyst particle mass balance with an effectiveness factor [55].

5. Conclusions

From the simulations with the developed dynamic HDT reactor model, the following conclusions can be pointed out:

- It is possible to simulate the most important HDT reactions simultaneously, provided that adequate kinetic model parameters are determined from experimental data.
- No wrong-way behavior is found when the reactant profiles along the catalyst bed in the first section of the reactor have a pronounced reduction or sharply slope.
- It is not necessary to take into account the gas phase in the heat balance, since only the solid and liquid phase heat balance equations or even with a single pseudohomogeneous heat balance equation is enough to predict the increase of reactor temperature along the reactor length.

Table 3

Values of effectiveness factors for the various reactions at steady-state.^a

Reaction	Axial position (cm)				
	0	213.4	426.7	640.1	853.4
HDS	0.64	0.70	0.84	0.90	0.93
HDN	0.88	0.81	0.71	0.62	0.58
HDA _{Poly}	0.90	0.81	0.75	0.70	0.67
HDA _{Pi}	0.88	0.82	0.77	0.73	0.70
HDA _{Mono}	0.98	0.98	0.98	0.98	0.98
HGO	0.88	0.92	0.93	0.93	0.93
HCR	1.0	1.0	1.0	1.0	1.0

^a $T_0 = 340^\circ\text{C}$, $P = 5.3\text{ MPa}$, $\text{LHSV} = 2.5\text{ h}^{-1}$, $\text{gas/oil ratio} = 356\text{ std m}^3/\text{m}^3$.

- The proposed dynamic heterogeneous model can be used as a tool to estimate kinetic parameters for further simulation of HDT reactors.

Acknowledgments

The authors thank Instituto Mexicano del Petróleo for its financial support. F.S.M. and I.E. also thank the financial support provided by CONACyT.

References

- [1] European standard for gasoline EN 228:1999 and for diesel EN 590:2004.
- [2] R.L. Irvine, D.M. Varraveto, *PTQ Summer* (1999) 37–44.
- [3] A.P. Lamourelle, D.E. Nelson, J. McKnight, *PTQ Summer* (2001) 51–56.
- [4] R.E. Palmer, S.P. Torrisi, *PTQ Revamps Operations* (February) (2004) 15–18.
- [5] R. Chowdhury, E. Pedernera, R. Reimert, *AIChE J.* 48 (1) (2002) 126–135.
- [6] M. Bhaskar, G. Valavarasu, A. Meenakshisundaram, K.S. Balaraman, *Pet. Sci. Technol.* 20 (3–4) (2002) 251–268.
- [7] G.F. Froment, G.A. Depauw, V. Vanrysselberghe, *Kinetic Modeling*, *Ind. Eng. Chem. Res.* 33 (12) (1994) 2975–2988.
- [8] D.E. Mears, *Chem. Eng. Sci.* 26 (9) (1971) 1361–1366.
- [9] H.C. Henry, J.B. Gilbert, *Ind. Eng. Chem. Proc. Des. Dev.* 12 (3) (1973) 328–334.
- [10] M.P. Duduković, *AIChE J.* 23 (6) (1977) 940–944.
- [11] H. Korsten, U. Hoffmann, *AIChE J.* 42 (5) (1996) 1350–1360.
- [12] D.G. Avraam, I.A. Vasalos, *Catal. Today* 79–80 (1–4) (2003) 275–283.
- [13] E. Pedernera, R. Reimert, N.L. Nguyen, V. van Buren, *Catal. Today* 79–80 (1–4) (2003) 371–381.
- [14] M. Bhaskar, G. Valavarasu, B. Sairam, K.S. Balaraman, K. Balu, *Ind. Eng. Chem. Res.* 43 (21) (2004) 6654–6669.
- [15] Z.-M. Cheng, X.-C. Fang, R.-H. Zeng, B.-P. Han, L. Huang, W.-K. Yuan, *Chem. Eng. Sci.* 59 (22–23) (2004) 5465–5472.
- [16] M.J. Macías, J. Ancheyta, *Catal. Today* 98 (1–2) (2004) 243–252.
- [17] S. Melis, L. Erby, L. Sassu, R. Baratti, *Chem. Eng. Sci.* 59 (22–23) (2004) 5671–5677.
- [18] M.A. Rodríguez, J. Ancheyta, *Energy Fuels* 18 (3) (2004) 789–794.
- [19] H. Yamada, S. Goto, *Korean J. Chem. Eng.* 21 (4) (2004) 773–776.
- [20] K. Sertić-Bionda, Z. Gomzi, T. Šarić, *Chem. Eng. J.* 106 (2) (2005) 105–110.
- [21] G.D. Stefanidis, G.D. Bellos, N.G. Papayannakos, *Fuel Process. Technol.* 86 (16) (2005) 1761–1775.
- [22] M. Oh, E.J. Jang, *J. Korean Inst. Chem. Eng.* (in Korean) 35 (5) (1997) 791–798.
- [23] J. Chen, Z. Ring, T. Dabros, *Ind. Eng. Chem. Res.* 40 (15) (2001) 3294–3300.
- [24] Y.-C. Chao, J.-S. Chang, *Chem. Eng. Comm.* 56 (1–6) (1987) 285–309.
- [25] M.A. Hastaoglu, B.E. Jibril, *Chem. Eng. Comm.* 190 (2) (2003) 151–170.
- [26] I. Iliuta, Z. Ring, F. Larachi, *Chem. Eng. Sci.* 61 (4) (2006) 1321–1333.
- [27] P.R. Gunjal, V.V. Ranade, *Chem. Eng. Sci.* 62 (18–20) (2007) 5512–5526.
- [28] F.S. Mederos, M.A. Rodríguez, J. Ancheyta, E. Arce, *Energy Fuels* 20 (3) (2006) 936–945.
- [29] F.S. Mederos, J. Ancheyta, *Appl. Catal. A General* 332 (1) (2007) 8–21.
- [30] M.S. Rana, J. Ancheyta, P. Rayo, S.K. Maity, *Catal Today* 98 (2004) 151–160.
- [31] J. Chen, V. Mulgundmath, N. Wang, *Ind. Eng. Chem. Res.* 50 (2011) 1571–1579.
- [32] A. Akgerman, G.M. Collins, B.D. Hook, *Ind. Eng. Chem. Fundam.* 24 (1985) 396–401.
- [33] S.M. Walas, *Modeling with Differential Equations in Chemical Engineering*, Butterworth-Heinemann, Boston, MA, USA, 1991, 450 pp.
- [34] W.E. Schiesser, *The Numerical Method of Lines – Integration of Partial Differential Equations*, Academic Press, Inc., San Diego, CA, USA, 1991, 326 pp.
- [35] A. Stanislaus, B.H. Cooper, *Catal. Rev. Sci. Eng.* 36 (1) (1994) 75–123.
- [36] S.B. Jaffe, *Ind. Eng. Chem. Proc. Des. Dev.* 13 (1) (1974) 34–39.
- [37] T.C. Ho, D. Nguyen, *Chem. Eng. Comm.* 193 (2006) 460–477.
- [38] O. Levenspiel, *Chemical Reaction Engineering*, third ed., John Wiley and Sons, Inc., New York, USA, 1999, 668 pp.
- [39] Software “Polymath”, Version 5.1, Numerical Solutions for Engineering and Science Problems, Cache Corp., Internet direction: <http://www.polymath-software.com> (accessed January 15, 2010).
- [40] B. Carnahan, H.A. Luther, J.O. Wilkes, *Applied Numerical Methods*, John Wiley and Sons, Inc., New York, USA, 1969, 604 pp.
- [41] B.H. Cooper, B.B.L. Donnis, *App. Catal. A General* 137 (2) (1996) 203–223.
- [42] Software “Matlab”, Release 2008a, The Language of Technical Computing, The MathWorks Inc., Internet direction: <http://www.mathworks.com> (accessed January 15, 2010).
- [43] G.F. Froment, K.B. Bischoff, J. De Wilde, *Chemical Reactor Analysis and Design*, 3rd ed., Wiley, New York, USA, 2010, 860 pp.
- [44] B.H. Cooper, B.B.L. Donnis, B. Moyse, *Hydroprocessing Conditions Affect Catalyst Shape Selection*, *OJG* 84 (December (49)) (1986) 39–44.
- [45] R.B. Bird, W.E. Stewart, E.N. Lightfoot, *Transport Phenomena*, John Wiley & Sons, New York, USA, 2002, 895 pp.
- [46] C.N. Satterfield, *Mass Transfer in Heterogeneous Catalysis*, MIT Press, Cambridge, MA, 1970, 267 pp.
- [47] M.O. Tarhan, *Catalytic Reactor Design*, McGraw-Hill, New York, 1983, 372 pp.
- [48] C.N. Satterfield, *AIChE J.* 21 (2) (1975) 209–228.
- [49] A. Bondi, *Chem. Tech.* 1 (1971) 185–188.
- [50] F. Mederos, I. Elizalde, J. Ancheyta, *Catal. Rev. Sci. Eng.* 51 (2009) 485–607.
- [51] J. Carberry, A. Varma, *Chemical Reaction and Reactor Engineering*, Chemical Industries/26, Marcel Dekker, New York, USA, 1987, 1069 pp.
- [52] F. Jiménez, K. Ojeda, E. Sánchez, V. Karafiov, R. Maciel Filho, in: V. Plesu, P.S. Agachi (Eds.), *17th European Symposium on Computer Aided Process Engineering–ESCAPE17*, Elsevier B.V., The Netherlands, 2007, pp. 1–6.
- [53] Z. Liu, Y. Zheng, W. Wang, Q. Zhang, L. Jia, *Appl. Catal. A General* 339 (2) (2008) 209–220.
- [54] J.G. Schwartz, G.W. Roberts, *Ind. Eng. Chem. Proc. Des. Dev.* 12 (3) (1973) 262–271.
- [55] T. Salmi, J. Wärnå, S. Toppinen, M. Rönholm, J.P. Mikkola, *Braz. J. Chem. Eng.* 17 (4–7) (2000) 1023–1035.
- [56] S. Ueda, S. Yokohama, T. Ishii, K. Makino, G. Takeya, *Ind. Eng. Chem. Proc. Des. Dev.* 14 (4) (1975) 493–499.